# LANGMUIR

## Biological and Environmental Phenomena at the Interface

## Hierarchical rose-petal surfaces delay the early-stage bacterial biofilm growth

yunyi cao, Saikat Jana, Leon Bowen, Xiaolong Tan, Hongzhong Liu,
Nadia Rostami, James Brown, Nicholas S. Jakubovics, and Jinju Chen

### Just Accepted

# Hierarchical rose-petal surfaces delay the early-stage bacterial biofilm growth

Yunyi Cao[†], Saikat Jana[†], Leon Bowen[‡], Xiaolong Tan[ℓ], Hongzhong Liu[§], Nadia Rostami[ǂ], James Brown[#], Nicholas S. Jakubovics[ǂ] and Jinju Chen[†]*

[†] School of Engineering, Newcastle University, Newcastle Upon Tyne, NE1 7RU, UK; [‡] Department of Physics, Durham University, Durham, DH1 3LE, UK; [ℓ] School of Pharmacy, Newcastle University, Newcastle Upon Tyne, NE1 7RU, UK; [§] School of Mechanical Engineering, Xi'an Jiaotong University, Xi'an 710054;. [ǂ] School of Dental Sciences, Newcastle University, Newcastle Upon Tyne, NE2 4BW, UK; [#]Centre for Biomolecular Sciences, University of Nottingham, Nottingham, NG7 2RD, UK.

## ABSTRACT

A variety of natural surfaces exhibit antibacterial properties; as a result significant efforts in the past decade have been dedicated towards fabrication of biomimetic surfaces that can help control biofilm growth. Examples of such surfaces include rose petals, which possess hierarchical structures like the micro-papillae measuring tens of microns and nano-folds that range in the size of 700 ±100 nm. We duplicated the natural structures on rose-petal surfaces via a simple UV-curable nanocasting technique, and tested the efficacy of these artificial surfaces in preventing biofilm growth using clinically relevant bacteria strains. The rose-petal structured surfaces exhibited hydrophobicity (contact angle~130.8º ±4.3º) and high contact angle hysteresis (~91.0° ±4.9°). Water droplets on rose-petal replicas evaporated following the constant contact line mode, indicating the likely coexistence of both Cassie and Wenzel states (Cassie-Baxter impregnating wetting state). Fluorescent microscopy and image analysis

1

26  revealed the significantly lower attachment of *Staphylococcus epidermidis* (86.1± 6.2% less)

27  and *Pseudomonas aeruginosa* (85.9 ±3.2% less) on the rose-petal structured surfaces,

28  compared with flat surfaces over a period of 2 hours. Extensive biofilm matrix was observed

29  in biofilms formed by both species on flat surfaces after prolonged growth (several days), but

30  was less apparent on rose-petal biomimetic surfaces. In addition, the biomass of *S. epidermidis*

31  (63.2 ±9.4% less) and *P. aeruginosa* (76.0 ±10.0% less) biofilms were significantly reduced

32  on the rose-petal structured surfaces, in comparison to the flat surfaces. By comparing *P.*

33  *aeruginosa* growth on representative unitary nano-pillars, we demonstrated that hierarchical

34  structures are more effective in delaying biofilm growth. The mechanisms are two-fold: 1) the

35  nano-folds across the hemispherical micro-papillae restrict initial attachment of bacterial cells

36  and delay the direct contacts of cells via cell alignment, and 2) the hemispherical micro-papillae

37  arrays isolate bacterial clusters and inhibit the formation of a fibrous network. The hierarchical

38  features on rose petal surfaces may be useful for developing strategies to control biofilm

39  formation in medical and industrial contexts.

40

## 1. INTRODUCTION

42  Bacteria are ubiquitous in the environment and can adhere onto abiotic or biotic surfaces to

43  form biofilms[1]. These three-dimensional (3D) communities of sessile cells are encased in a

44  matrix of extracellular polymeric substances (EPS). Biofilms can be useful in biotechnological

45  processes such as bioremediation, biofertilizers, and in microbial fuel cells[1]. By contrast,

46  certain biofilms can be detrimental to human health, causing infections and diseases[1-2]. It has

47  been estimated that up to 80% of bacterial infections in humans are biofilm associated, and

48  biofilms are responsible for the majority of hospital-acquired infections. Biofilm associated

49  infections are the fourth leading cause of death worldwide, within the U.S. about 2 million

50  annual cases lead to more than $5 billion USD in added medical costs per annum[3-5]. In the UK,

51  about 300,000 people per annum in England suffer from hospital-acquired infections under

52  NHS care and the costs also run into billions of pounds[6]. Hence, it is important to investigate

53  techniques that can control biofilm growth and reduce the instances of infections. Bacterial

54  biofilms are robust structures and are difficult to treat via traditional antibiotic therapy[5-7]. The

55  EPS matrix acts as a barrier to agents trying to access the interior of the biofilm, subsequently

56  triggering the development of antibiotic resistance[7], which has been shown for both

57  *Staphylococcus epidermidis*[5] and *Pseudomonas aeruginosa*[8]. Physical strategies, in particular

58  the use of rationally designed surface topographies, have gained interests and present us with

2

59  an interesting approach to prevent bacterial adherence and biofilm growth without the

60  requirement for antimicrobials[9-10].

61  Natural surfaces with micro/nano topographical patterns have inspired researchers to design

62  artificial biomimetic surfaces to control biofilm growth. For example, lotus leaf has

63  hierarchical structures such as micro-papillae (measuring ~3–11 μm diameter) that are

64  randomly covered by nano-tubules (~100 nm diameter)[11-12]. Water droplets on these surfaces

65  cannot penetrate the air pockets formed within the hierarchical structures (i.e. Cassie state)[11-12]

66  . As a result the lotus leaf is found to exhibit superhydrophobicity with a contact angle (CA)

67  >150° and a low contact angle hysteresis (CAH) (i.e. <10°), which results in the easy rolling

68  off of water droplets (i.e. self-cleaning effects) [12-14].  However, it is challenging to reproduce

69  the hierarchical structures on lotus leaf in the laboratory[15-17]. Using lotus leaf as a template, it

70  has only been possible to fabricate unitary structures based on the micro-papillae; the nano-

71  tubules are too small for this approach[18-23]. Hierarchical structures similar to the lotus leaf can

72  be generated using chemical processes, but these are not exactly the same structures as found

73  on natural lotus leaves[24-27]. Nevertheless, lotus leaf-inspired superhydrophobic surfaces

74  (unitary structure or hierarchical structures) can mitigate biofouling by a range of bacteria

75  including *Staphylococcus aureus*, *S. epidermidis*, *P. aeruginosa* and *Planococcus maritimus*,

76  since the trapped air restricts the direct contact between the solid surfaces and micro-

77  orgasisms[18, 20-21]. The anti-fouling efficacy strongly depends on the lifetime of non-wetting

78  (Cassie) state. The wetting transition (Cassie to Wenzel state) can occur within 1-4 hours in

79  submerged environments, with a significant decrease in CA and  increase in CAH[10, 18]. Bacteria

80  can also accelerate such transitions, for example by flagella-mediated motility[10]. Therefore, it

81  is commonly accepted that surface topography features such as size, pitch or height play a

82  primary role in delaying bacterial attachment or biofilm growth and that wettability (CA and

83  CAH) is less important, especially when surfaces get fully wetted[5, 10, 20, 28].

84  Different surface topographies on many other natural surfaces including rice leaves[29], shark-

85  skin[30-32], gecko-skin[9, 33-34], cicada wings[5, 35-36], or dragonfly wings[37-38] have also been

86  demonstrated to have anti-biofilm properties to different levels. Topographical features larger

87  than bacterial cells, such as the microstructures in Sharklet AF[TM], constrain bacterial deposition

88  to recessed regions and delay biofilm formation[32]. Topographies close in size to bacteria can

89  lead to alignment of rod-shaped bacterial cells between the surface features and retard biofilm

90  formation, possibly by blocking cell-cell communications[39-42]. By contrast, features such as

91  tightly-spaced nano-spears that are smaller than bacterial cells can delay surface attachment

3

92   without necessarily restricting biofilm formation to a great extent [5, 10]. Previous investigations

93   have reported that rose petals have hierarchical structures with micro-papillae (~20 μm

94   diameter) and nano-sized cuticular folds (~730 nm width)[43-44]. Such hierarchical structures

95   make the rose-petal surface superhydrophobic even allowing it to exert a high adhesive force

96   on droplets[43]. A few studies examined the dynamics of water droplets and efficacy of the

97   structured surfaces in preventing bacterial growth[43-44]. However, the mechanism responsible

98   for the inhibition of bacterial growth by the rose-petal structures is not well-understood. There

99   was also lack of study about how such structures may affect bacteria alignment and biofilm

100  formation.

101  The present study focuses on investigating bacterial attachment and early-stage biofilm

102  formation on biomimetic rose-petal surfaces. The imprints of rose-petal hierarchical structures

103  were fabricated via nanocasting technique. The wettability of rose-petal replicas were accessed

104  by the static/dynamic contact angle measurement and droplet evaporation tests. By using

105  fluorescent microscopy and scanning electron microscope (SEM), growth of two clinically

106  relevant biofilm forming strains *S. epidermidis* and *P. aeruginosa* were evaluated on the rose-

107  petal-structured and flat surfaces. In addition, by comparing the growth of *P. aeruginosa* on

108  the model unitary nano-pillar structures, we demonstrated the efficacy of hierarchical structures

109  in delaying biofilm growth.

110

## 2. MATERIALS AND METHODS

111

112  **2.1 Surface fabrication:** One piece of fresh rose petal (Figure 1a) was attached to a glass slide

113  (1 cm ×1 cm) via a double-sided adhesive tape (Figure 1b). A mixture of Poly(dimethylsiloxane)

114  (PDMS) and its curing agent was prepared from SYLGARD 184 Elastomer Kit (Dow Corning

115  Corporation, Midland, MI) with a ratio of 10:1 (wt/wt). The solution was thoroughly mixed

116  and degassed in a vacuum chamber for 30 minutes to eliminate air bubbles. The mixture was

117  poured over the glass slide with rose petals in a Petri dish (Figure 1c), and cured at room

118  temperature for 48 hours. After curing, the PDMS mould was gently peeled off which left a

119  negative imprint of the structures on the petal (Figure 1d). UV-curable epoxy (OG 142-87,

120  Epoxy Technology, Inc.) was poured onto the negative imprint of the PDMS mould and was

121  gently covered with a pre-cleaned glass slide (1 cm ×1 cm) as a substrate. The UV-curable

122  epoxy was cured under a UV-lamp, with the luminous intensity of 100 mW/cm² and the

123   wavelength of 365 nm, for 20–25 minutes until fully cured (Figure 1e). After cooling to room

124   temperature, the cured epoxy was demoulded by bending the PDMS mould (Figure 1f).

125   To better understand the advantage of the hierarchical structures over the unitary structures, a

126   similar technique was used to produce periodic nano-pillar structures (diameter ~500 nm, pitch

127   ~1 μm, height ~2 μm) with the same materials. More details can be found in the Supporting

128   Information.
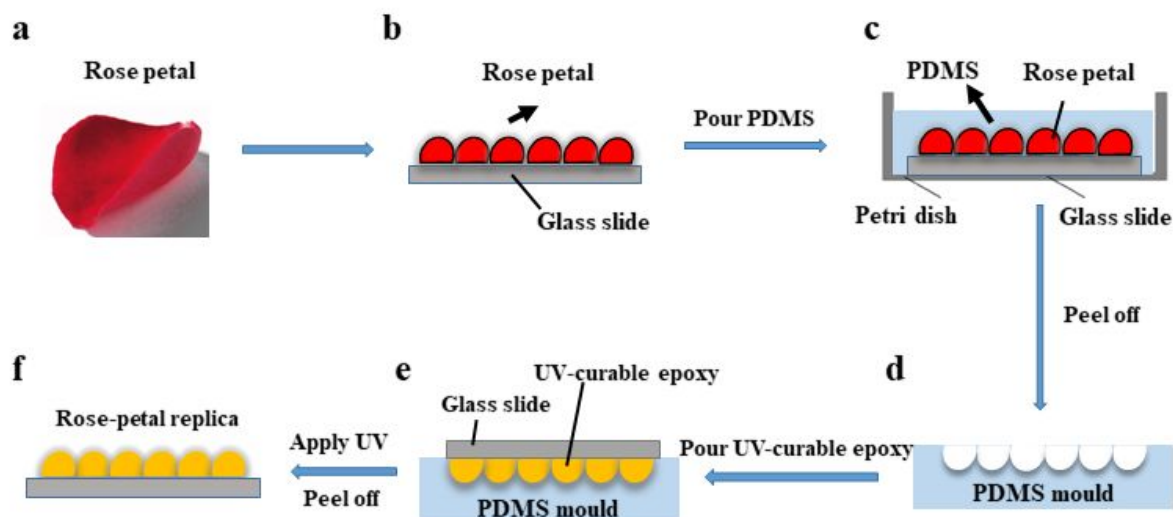


129

130   **Figure 1.** Schematic of the fabrication method to obtain rose-petal replicas.

131   **2.2 Characterization of rose-petal structured surfaces:** The replicas of rose-petal surfaces

132   were imaged using a scanning electron microscope (SEM). FEI Helios NanoLab 600

133   DualBeam system was operated at an acceleration voltage of 5 KV, which allowed to get good

134   magnifications, while will not damage the surfaces. We also measured the contact angles (CA)

135   on flat and rose-petal-structured epoxy surfaces by placing a sessile drop of 3 μl deionized

136   water (i.e. DI water), and evaluated by a CAM 100 optical contact angle meter (KSV

137   Instruments Ltd., Finland). To characterize the evaporation dynamics, a 3 μl DI water droplet

138   was placed on either of the surfaces, and their intensity projections were captured every 300

139   seconds by the optical contact angle meter. The droplet edges were extracted by an in-house

140   Matlab code and plotted in a single image to visualize the droplet transitions overtime. An in-

141   house goniometer[45-46] was set-up to measure the advancing contact angles on flat and rose-

142   petal surfaces using a syringe-pump system (needle gauge ~25, water droplet volume ~10 μl,

143   dispensing rate~ 0.2 ml/minute). Receding contact angles were also measured using the same

144   method with the syringe pump operating in withdrawal mode. All the measurements were

145 repeated for three instances and the images were processed using ImageJ. Results are presented

146 as the mean contact angles with standard deviations.

147 **2.3 Bacteria culture, attachment and biofilm growth:** Biofilm-forming strains of *S.*

148 *epidermidis* FH8 and *P. aeruginosa* PAO1-mCherry were used in this study[47-49]. *S. epidermidis*

149 FH8 was isolated from a chronic rhinosinusitis patient at the Freeman Hospital, Newcastle

150 Upon Tyne[49]. PAO1-mCherry is the derivative of *P. aeruginosa* PAO1-N (Nottingham

151 subline[50]), which was engineered via chromosomal insertion (attTn7::ptac-mcherry) to

152 constitutively express a red fluorescent protein mCherry. *S. epidermidis* FH8 and *P. aeruginosa*

153 PAO1-mCherry were routinely cultured in Tryptic Soy Broth (TSB, Melford Laboratories Ltd,

154 UK), in an incubating shaker at 180 rpm, 37℃ for 16 hours and then used for experiments.

155 The optical density of *S. epidermidis* FH8 was measured by a spectrophotometer (Biochrom

156 Libra S11, Biochrom Ltd., Cambridge, UK) and diluted to $OD_{600}= 0.30$ with fresh TSB medium.

157 3 ml of the diluted bacterial culture was incubated with flat and rose-petal structured surfaces

158 in 12-well culture plates for 2 hours at 37℃ and then removed for visualization. To monitor

159 the early-stage biofilm formation, we cultured *Staphylococcus epidermidis* FH8 on flat/rose-

160 petal surfaces for up to 2 days. *P. aeruginosa* PAO1-mCherry colonizes surfaces rapidly.

161 Therefore, to avoid overloading the system, different culture conditions were selected for *P.*

162 *aeruginosa* with a lower bacterial inoculum ($OD_{600}= 0.01$) and incubation in 100x diluted TSB

163 for 2 hours (bacterial attachment assay) or 24 hours (biofilm formation assay) . This method

164 enabled biofilm growth to be visualised on the different surfaces without shielding the initial

165 surface structure.

166 **2.4 Fluorescent Microscope Analysis:** After the bacterial attachment assay or biofilm

167 formation assay, surfaces were gently rinsed three times with Phosphate Buffered Saline (PBS,

168 pH=7.4) to remove loosely adhered bacteria. Surfaces incubated with PAO1-mCherry were

169 directly visualized by fluorescent microscopy after washing. For *S. epidermidis* FH8, the

170 adherent bacteria or biofilms were stained with SYTO®9 (Invitrogen, Life Technologies,

171 Carlsbad, CA, USA) following the standardized methods. All surfaces were visualized using

172 an Olympus BX61 upright fluorescent microscope with a 20x objective. For the bacterial

173 attachment assay (2 hours), surfaces were examined (see Support Information) by acquiring

174 2D fluorescent images in a single focal plane ($121.25 \times 108.75$ μm$^2$). For biofilms, z-stacks

175 were performed through the thickness of biofilms from 5 random locations on the surfaces. The

176 biomass in each field of view ($430.00 \times 324.38$ μm$^2$) was determined using the COMSTAT2

177    plugin (Lyngby, Denmark) in ImageJ. Three independent experiments were performed for each

178    surface type.

179    **2.5 SEM Analysis:** Surfaces (with bacteria or biofilms) were washed three times with PBS and

180    fixed in 2% glutaraldehyde with 3M Sorenson's phosphate buffer, overnight at 4°C. Then they

181    were dehydrated through a series of ethanol solutions of 25% (v/v), 50%, 75%, and 100%,

182    followed by critical point drying (Leica EM CPD300). The dried surfaces (with bacteria or

183    biofilms) were sputter-coated with 16 nm platinum to increase the surface conductivity,

184    enabling higher resolution imaging by the SEM.

185    **2.6 Statistical Analysis:** Data are represented as mean values with standard error. Student's t-

186    test assuming unequal variations was applied and *$p < 0.05$ was considered statistically

187    significant in this study.

188

## 3. RESULTS AND DISCUSSION

189

### 3.1 Characterization of surface topography and wettability of rose-petal replicas

190

191    SEM imaging of the UV-epoxy rose-petal replicas (Figure 2 a1) revealed the existence of

192    periodic arrays of hemispherical micro-papillae in the diameter of 23 ±3 μm , similar to the

193    microstructures on natural rose petals (~ 20 μm)[43-44]. The magnified SEM images in Figure 2

194    a2 shows the existence of cuticular folds were found at the top of micro-papillae, closely

195    mirroring the hierarchical topographies of the natural rose petal. The width of each fold was

196    measured to be in the range of 700 ±100 nm, similar to the size as previously reported (~ 730

197    nm[43-44]) and the gap between each fold was measured to be 500 ±150 nm (Figure 2 a3).

198    Collectively, the rose-petal replicas exhibit as hierarchical structures with micro-papillae and

199    nano-folds in two different scales.

200    The static water contact angle (CA) on the flat surface was measured to be 60.5º ±6.5º (Figure

201    2b), indicating that the cured flat epoxy surface was intrinsically hydrophilic. For the rose-petal

202    replicas, the CA value on surfaces was measured to be 130.8º ±4.3º (Figure 2b), indicating that

203    the hierarchical structures had enhanced the surface hydrophobicity significantly. The water

204    droplets stayed pinned on rose-petal structured surfaces under different tilt angles ranging from

205    30 - 180° (Figure 2c), implying that there exist highly adhesive interactions between the drops

206    and the structured surfaces[43-44]. Contact angle hysteresis (CAH) measurement which is an

207    indicator of slipperiness (water-repellence), were conducted by using the dynamic CA method

208   (by increasing or decreasing the volumes of water droplets using a needle[51]). CAH (also defined

209   as the difference between the advancing and receding angle of a water droplet) of the rose-petal

210   structured surfaces (91.0° ±4.9°) was measured to be significantly higher than that of the flat

211   surfaces (44.8° ±4.3°), as shown in Figure 2b. This indicates the presence of a large number of

212   pinning points on rose-petal structured surfaces, which cause the adhesion of liquid droplets.

213   We also evaluated the evaporation dynamics of water droplets on these two surfaces (Figure

214   2d), as CAH has been attributed to be the main factor affecting drop evaporation[52]. Figure e-f

215   shows the evolution of CA and contact radius of a water droplet during the evaporation process.

216   For the flat surface, the evaporation started with the constant contact line (CCL) mode up to

217   900s (Figure f): the CA decreased, while the contact radius remained constant. After that, the

218   CA decreased to its receding CA (i.e. 37.6° ± 4.5° in this study), and contact line started to

219   recede. The CA remained almost constant ranging from 900-1500s (Figure e), indicating that

220   this is the constant contact angle (CCA) mode during this period of time. At the end of

221   evaporation (1500-1800s), both CA and contact radius decreased (i.e. mixed mode) as shown

222   in Figure f. This observation was consistent with the normal evaporation process which was

223   reported on smooth hydrophilic surfaces[53]. By contrast, rose-petal structured surfaces exhibited

224   mostly as CCL mode over time (Figure d &f & S1) due to its higher CAH. The CA of rose-

225   petal surfaces require more time to decrease to its receding CA (i.e. 37.2° ± 4.3° in this study).

226   Therefore, the contact line is pinned and contact radius keeps constant during the evaporation.

227
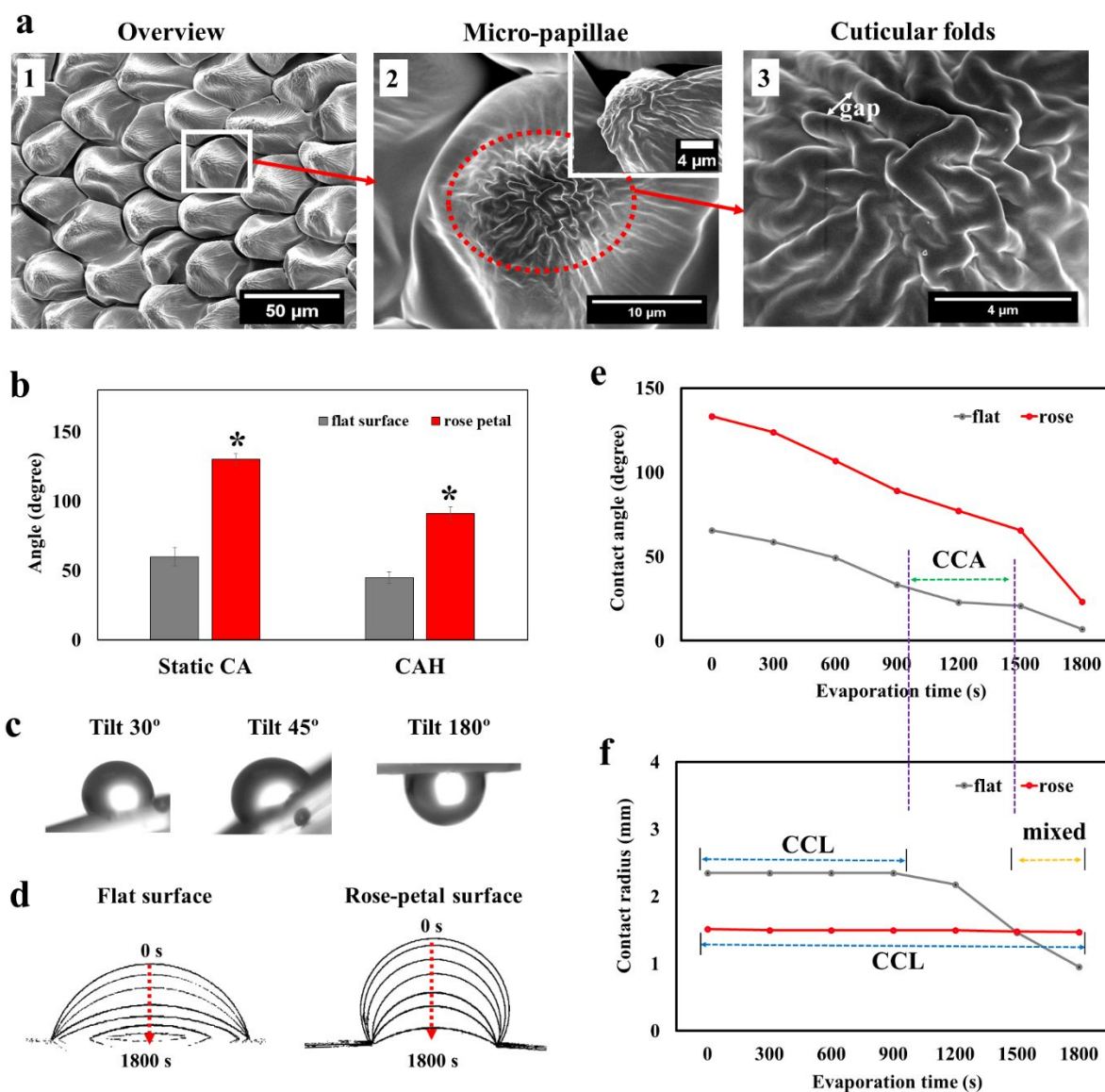


**Figure 2. (a)** SEM images of the rose-petal replicas made by UV-epoxy. (a1) an overview of the hierarchical structures on surface, taken at 1000x. (a2) A typical SEM image taken at 8000x showing the hemispherical micro-papillae with cuticular folds, and the inset was taken at 20° tilt with the magnification of 12000x. (a3) The magnified SEM image taken at 25000x showing the detailed cuticular nano-folds. **(b)** Static water contact angle (CA) and contact angle hysteresis (CAH) measurements on flat and rose-petal structured surfaces, *$p$=6.7×10$^{-6}$ for CA and *$p$=2.0×10$^{-13}$ for CAH. **(c)** Digital images of 3 μl water droplets on the rose-petal structured surfaces under different tilt angles. **(d)** A typical example of the edges of 3 μl water droplets, when evaporated on the flat and rose-petal structured surfaces overtime. The outside of droplet edge was extracted at the time of 0 s, and the time interval between each edge was 300 s. **(e-f)**

9

239    Evolution of contact angle (f) and contact radius (g) of water droplets (3 μl) evaporating on flat

240    and rose-petal structured surfaces.

241    The evaporation process on rose-petal replicas didn't agree with the normal observations of

242    hydrophobic surfaces, which is dominated by CCA mode as previously reported[52-53]. The

243    normal hydrophobic or superhydrophobic surface like lotus leaf allows air to remain inside the

244    texture (i.e. Cassie state), thereby have a low CAH. This results in the evaporation process

245    follows as CCA mode with the easy receding of contact line[53]. However, it is believed that

246    there have the coexistence of air pockets and water–solid contacts on rose-petal surface. This

247    results in Cassie and Wenzel states coexist on rose-petal-like surfaces (also known as Cassie-

248    Baxter impregnating wetting state[43-44]). Therefore, rose-petal surface is hydrophobic but have

249    a high CAH[54]. This special wetting state is attributed to the hierarchical micro- (i.e. arrays of

250    papillae) and nanostructures (i.e. cuticular folds) on rose-petal surface. The relatively large and

251    periodic arrays of papillae can exert a capillary force that facilitates the penetration of water

252    into papillae valleys[55]. However, the water cannot enter into the nanoscale structures (i.e.

253    cuticular folds) at the top where tapped air pockets exist. This kind of special wetting state on

254    the rose-petal surfaces is also termed as the "petal effect" and has been well investigated by

255    researchers[43-44, 55].

256

### 3.2 Bacterial adherence is delayed by the rose-petal structured surfaces

258    We initially assessed the attachment of two common human pathogens, *S. epidermidis*

259    (spherical-shape) and *P. aeruginosa* (rod-shape) on the different surfaces after 2 hours. A

260    standard practice for counting planktonic cells is measuring colony forming units (CFU)[56].

261    However, this is not straightforward for enumeration of bacteria in biofilms on patterned

262    surfaces owing to difficulties of removing all cells from the surface and breaking up aggregates

263    into single cells without killing them[5, 56]. Therefore, fluorescence microscopy and quantitative

264    image analysis was employed to enumerate bacterial cells in biofilms and to assess their

265    distributions on the surface.

266    The distribution of fluorescence signals (green for *S. epidermidis* and red for *P. aeruginosa*)

267    was relatively uniform on the flat surfaces, indicating that the bacterial cells had attached

268    uniformly across the surface (Figure 3 a1&3). However in the case of rose-petal structured

269    surfaces, the fluorescent patches of *S. epidermidis* or *P. aeruginosa* were sparsely scattered,

270    and large areas without fluorescent signal were observed. This indicated that cells were only

10

able to attach to specific regions on the rose-petal structure (Figure 3 a2&4). Figure 3b shows

that the surface area covered by *S. epidermidis* and *P. aeruginosa* on rose-petal structured

surface, which was significantly lower (86.1± 6.2% less and 85.9 ±3.2% less, respectively) in

comparison to the area covered by bacteria on flat surfaces. It is possible that the wash steps

passing through the air-liquid interfaces may have selectively removed relatively weakly

attached cells and affected the distribution of cells on surfaces[57]. Therefore, control

experiments were performed where samples were never passed through an air-water interface

and were imaged using a water dipping lens. The distribution of cells was very similar to those

seen in washed samples (data not shown), indicating that forces exerted during wash steps do

not have a major impact on attached bacterial cells. Overall, the observations indicate that the

rose-petal structures have the ability to inhibit the initial bacterial attachment.
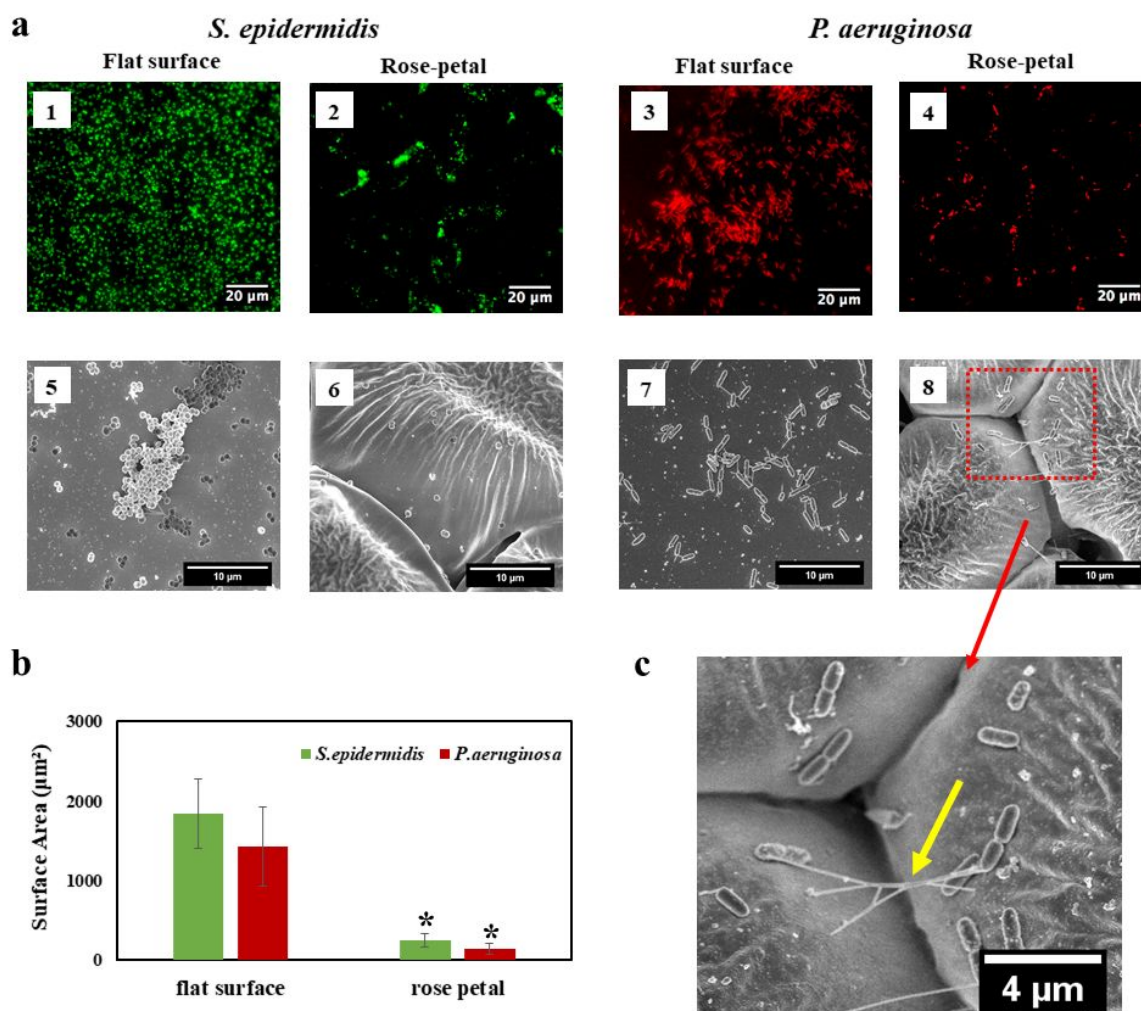


**Figure 3.** Adherence of *S. epidermidis* and *P. aeruginosa* on different surfaces after 2 hours'

incubation. **(a)** Fluorescent microscopy (1-4) and SEM (5-8) images of *S. epidermidis* and *P.*

*aeruginosa* on flat and rose-petal structured surfaces. **(b)** The surface area coverage of each

286   type of bacteria in the field of view ($121.25 \times 108.75 \ \mu m^2$) for each surface was determined by

287   ImageJ. *$p$=2.1×10$^{-9}$ for *S. epidermidis* and *$p$=5.1×10$^{-11}$ for *P. aeruginosa*. **(c)** A zoomed in

288   view of the cross-section in a8 showed the existence of cellular appendages (yellow arrow),

289   which might mediate bacterial attachment of *P. aeruginosa*, by connecting isolated cells.

290   To investigate the interactions at a higher spatial resolution, SEM was used to visualize *S.*

291   *epidermidis/ P. aeruginosa* on different surfaces. On flat surfaces, *S. epidermidis* tended to

292   cluster into small aggregates (Figure 3 a5). By contrast, on the rose-petal surfaces, which

293   comprised of hierarchically arranged micro- (i.e. arrays of papillae) and nanostructures (i.e.

294   cuticular folds), 85.6 ±5.8% of *S. epidermidis* cells (based on SEM images, n=9) were localized

295   in the valleys or crevices between micro-papillae (Figure 3 a6 & S2). Cells were not commonly

296   seen at the top of the micro-papillae. These observations were consistent with the acquired

297   fluorescent images (Figure 3 a2&4), where large areas without fluorescent cells were seen and

298   presumably represented the sites of nano-folds. We did not observe cell aggregates of *S.*

299   *epidermidis* on rose-petal surface and found that most of the attached cells were isolated

300   (Figure 3 a6 & S2). Similar observations were also found for *P. aeruginosa*, as shown in Figure

301   3 a7-8 & S3. In this case, 90.4 ±3.1% of cells (based on SEM images, n=9) were present in the

302   valleys. The major difference between the cell types was that *P. aeruginosa* cells were

303   connected by long tube-like appendages, which may have mediated cellular attachment by

304   connecting the isolated cells together (Figure 3c).

305

### 3.3 Biofilm growth is delayed by the rose-petal structured surfaces

### 3.3.1 Biofilm growth of *S. epidermidis* on different surfaces

308   To investigate whether the rose-petal structures are effective in delaying biofilm growth, *S.*

309   *epidermidis* biofilms were cultured for 2 days and then analysed using fluorescent microscopy

310   as well as SEM (Figure 4). Maximum intensity projections through the thickness of *S.*

311   *epidermidis* biofilms showed bright patches on the flat surface (Figure 4 a1), indicating a

312   typical biofilm growth comprising multiple layers of cells. Few smaller green patches were

313   observed on the rose-petal structured surface, which appeared as circular or oval structures with

314   centrally located dark regions that lacked fluorescence (Figure 4 a2). The diameter of these

315   circular regions were measured to be 21 ± 4 μm, which is similar to the dimensions of

316   hemispherical micro-papillae (i.e. 23 ± 3 μm in diameter) on the rose-petal structures. This

317   indicates that *S. epidermidis* clusters/biofilms preferentially form around the micro-papillae.

318    The total biomass on the rose-petal surface was significantly lower (63.2 ±9.4% less) compared

319    with the biomass on the flat surface (see Figure 4c), indicating that rose-petal structure can

320    delay the biofilm growth. A dense biofilm network was observed on the flat surface, and string-

321    like structures consisting of filamentous fibrils appeared to bridge *S. epidermidis* cells together

322    (Figure 4 b1&2). These filamentous fibrils are known to be part of EPS structure of *S.*

323    *epidermidis* biofilms[58] which indicates a more mature biofilm growth. By contrast, no

324    filamentous fibrils were observed on the rose-petal surfaces (Figure 4 b3&4). A few cellular

325    clusters were sparsely scattered on the rose-petal structure and the majority of cells occupied

326    the valleys between the micro-papillae (Figure 4 b3 & S4), consistent with the findings of

327    fluorescent imaging (Figure 4 a2) which revealed cells preferentially surrounding the micro-

328    papillae. Small aggregates of around ~20 cells were observed on the cuticular folds (Figure 4

329    b4), however 3D clusters or aggregates on the cuticular folds at the top of micro-papillae were

330    relatively rare. The diameter of *S. epidermidis* cells were measured to be 700 ±70 nm in this

331    study, which is of similar dimensions compared to the feature size of folds (width ~700 ±100

332    nm, gap ~500 ±150 nm). *S. epidermidis* cells can deposit into these fold gaps thereby forming

333    small aggregates at the top of micro-papillae over time (Figure S4).
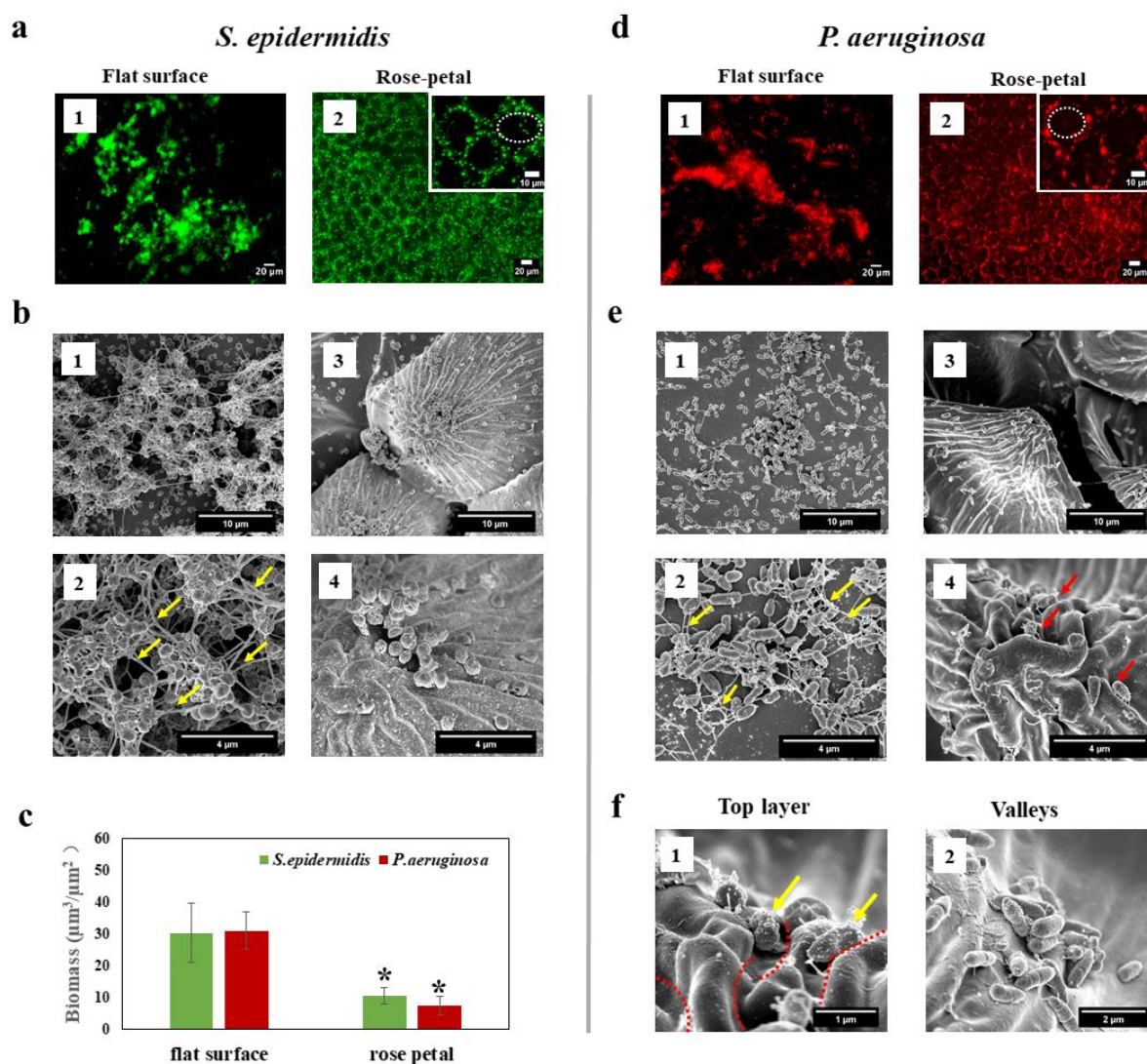
**Figure 4.** Biofilm formation (2 days) on the flat and rose-petal structured surfaces. **(a)** Fluorescent images of *S. epidermidis* biofilms on different surfaces. The cells on the rose-petal surfaces are distributed in oval shaped patterns which is highlighted by a dashed white line in a2. **(b)** SEM images of *S. epidermidis* biofilms on different surfaces. b1 and b3 are lower magnification images; b2 and b4 are high magnifications. Yellow arrows indicate the filamentous fibrils from the EPS of biofilms. **(c)** Biomass volume per unit area on the different surfaces calculated from ImageJ Comstat2. *$p$=1.8×10$^{-6}$ for *S. epidermidis* and *$p$=3.8×10$^{-11}$ for *P. aeruginosa*. **(d)** Fluorescent images showing *P. aeruginosa* biofilms on different surfaces. The dashed white line highlights a cuticular region, with cells distributed in a circular pattern around the edge of micro-papillae. **(e)** SEM images of *P. aeruginosa* biofilms on different surfaces at lower magnifications (e1 and e3) and higher magnifications (e2 and e4). Yellow arrows indicate the filamentous fibrils from the EPS of biofilms and red arrows indicate the isolated bacterial cells within the cuticular folds. **(f)** High-magnification SEM images of *P.*

348    *aeruginosa* biofilms on rose-petal surface, yellow arrows indicate the bacterial alignment

349    within the cuticular nano-folds, and red dash lines indicate the boundary of folds, as shown in

350    f1. *P. aeruginosa* aggregates can form in the valleys of micro-papillae, as shown in f2.

351

### 3.3.2 Biofilm growth of *P. aeruginosa* on different surfaces

353    Maximum intensity projections through the thickness of *P. aeruginosa* biofilms and the

354    corresponding SEM images of the different surfaces are shown in Figure 4 d-e. Circular or oval

355    shaped structures were observed in the fluorescent images of rose-petal surface (Figure 4 a4).

356    This indicates that *P. aeruginosa* biofilm preferentially grew in between micro-papillae, akin

357    to the growth mechanism of *S. epidermidis*. The total biomass of *P. aeruginosa* biofilms was

358    significantly reduced on the rose-petal structured surfaces (76.0 ±10.0% less), comparing to

359    the biomass on the flat surface (see Figure 4c). Figure 4e (1&2) shows the existence of *P.*

360    *aeruginosa* clusters with a developed network of filamentous fibrils surrounding the cell bodies

361    on the flat surface. In contrast to *S. epidermidis*, *P. aeruginosa* biofilms did not contain

362    significant aggregates or clusters on the rose-petal surface, possibly due to the lower initial

363    bacterial density and the nutrient-limited conditions arising from rapid cellular growth (Figure

364    4e 3 & S5). Most cells were found to be isolated on structured surfaces, in contrast to the flat

365    surface (Figure 4e). At a higher magnification, small bacterial aggregates were observed,

366    comprising ~10 cells in the valleys of micro-papillae on the rose-petal surface (Figure 4f 2 &

367    S5 b), without showing the long filamentous fibrils. *P. aeruginosa* cells were also occasionally

368    found attached within the cuticular nano-folds at the top of micro-papillae (Figure 4 e4& f1).

369    We measured the gap between folds to be 500 ±150 nm (Figure 2 a3) which is similar to the

370    diameter of *P. aeruginosa* and found that a single *P. aeruginosa* cell was capable of settling

371    into these gaps over time. The cells tended to align with the folds (Figure 4 f1 & S5 c-d) and

372    the preference for alignment along the nano-folds was strong even though the fold structure

373    was irregular. The crowns of the cuticular folds were visible after the long-term bacterial

374    growth (i.e. 24 hours), as the bacteria tended to remain confined in the ridges between the nano-

375    folds (Figure 4 f1 & S5 c-d). To further assess *P. aeruginosa* biofilm growth, the period of

376    biofilm development was extended to 48 hours - the same incubation time of *S. epidermidis*

377    biofilms. In these experiments, the biomass on rose-petal structured surface was also found to

378    be significantly lower (68.7 ± 13.4% less) in comparison of the biomass on the flat surface

379    (Figure S5). The observations confirm that the rose-petal structure was able to delay the early

380    stage biofilm growth of *P. aeruginosa*.

### 3.4 Bacterial growth of *P. aeruginosa* on unitary nano-pillars

We used a simpler surface pattern containing unitary nano-pillars to examine the alignment of *P. aeruginosa* and evaluate anti-microbial performance against the hierarchical rose-petal structures. The unitary nano-pillar structured surface was moderately hydrophobic (CA of 94.8°±3.7°) and the dimensions of the topographical features was similar to the nano-folds on rose-petals and comparable to the size of *P. aeruginosa* cells. Figure 5a and b1 showed that bacterial cells aligned with gaps between the nano-pillars after 2 hours, consistent with previous investigations[39]. Bacterial appendages tended to link to pillars (Figure 5b2). The total surface area covered by bacteria after 2 hours was significantly lower on the nano-pillar surface compared with the rose-petal surface (see Figure 5c&3b, 107.2±28.6 $\mu m^2$ vs 143.8±71.2 $\mu m^2$, $p$=0.012), possibly owing to the restricted area (pillar pitch) where bacteria can make the initial contacts to material surface. However, the biomass of *P. aeruginosa* after 24 hours (15.7±4.3 $\mu m^3/\mu m^2$, Figure 5c) on nano-pillars was significantly higher than on rose-petal replica surfaces (7.3±2.8 $\mu m^3/\mu m^2$, Figure 4c) ($p$=0.002). Bacteria continued to deposit into the nanopillar pitches, and dense filamentous fibrils were observed surrounding the cells, similar to the flat surfaces (Figure 5d2 and S7). However, the biomass on nano-pillars after 24 hours is still significant lower comparing to that on the flat surfaces (31.1±6.0 $\mu m^3/\mu m^2$, Figure 4c) ($p$= 2.7×10$^{-7}$), indicating that unitary nanostructures can still isolate cells and delay biofilm growth.
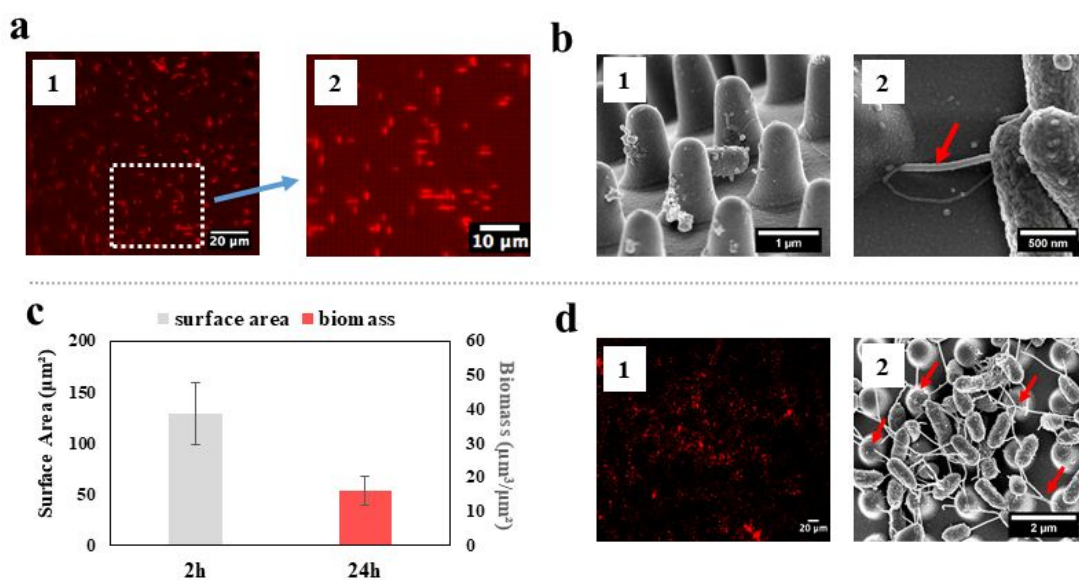


**Figure 5. (a)** Fluorescent microscopy and **(b)** SEM images of *P. aeruginosa* on nano-pillar surfaces after 2 hours, showing the cell patterning/aligning behaviour and a structure emanating from a bacterial cell (red arrow). **(c)** The surface area coverage (2 hours) and biomass (24 hours) of *P. aeruginosa* on nano-pillar surfaces. **(d)** Fluorescent microscopy and SEM images of *P.*

404    *aeruginosa* on nano-pillar surfaces after 24 hours, showing dense filamentous networks (red

405    arrows).

406

### 3.5 The mechanism of inhibiting biofilm growth on rose-petal surface

408    The efficiency of bacterial attachment on surfaces is dictated by chemical and physical

409    properties of surfaces[1]. We fabricated flat, rose-petal and nano-pillar structured surfaces using

410    a nanocasting technique with UV-curable epoxy, so the surface chemistry in each case can be

411    assumed to be the same. The major difference was the surface topographical features and this

412    was a critical determinant of bacterial attachment and biofilm growth.

413    We hypothesized that hierarchical structures (i.e. micro-papillae and nano-folds) on rose-petal

414    surfaces inhibit initial bacterial attachment after 2 hours. As a result of these structures, the

415    rose petal surface exhibits as a modified state of hydrophobicity, termed as the Cassie-Baxter

416    impregnating wetting state. The nanostructured cuticular folds can trap air within the folds,

417    corresponding to the Cassie-state of lotus-leaf; thereby bacterial cells cannot penetrate the air-

418    layer over short timeframes (Figure 6). This mechanism is similar to the lotus-leaf where the

419    trapped air restricts the direct contact between bacteria and surfaces. However, unlike the lotus-

420    leaf that has a low CAH, the papillae valleys can trap water thereby resulting in a high CAH.

421    Visualizing the bacteria-material interfaces under the Cassie impregnating wetting state which

422    combines wetting and non-wetting, is not an easy task. It may require sophisticated imaging

423    such as high-resolution Cryo FIB-SEM instead of conventional microscopy[59], especially down

424    to the 1μm scale. However, as seen in Figure 3, cells only preferentially colonize the valleys

425    surrounding the papillae and this region is also devoid of nano-folds. The hypothesis which

426    describes the lack of bacterial attachment within nano-folds (Figure 6) is consistent with our

427    observation of *S. epidermidis* and *P. aeruginosa* adherence behaviour on rose petal surfaces

428    (~2 hours).

429    If the bacterial growth extends to 1-2 days (biofilm assay), bacterial cells still only accumulate

430    surrounding the papillae forming ring/oval-like structures (Figure 6). The initial wetted micro-

431    papillae valleys can harbour more bacterial cells as they tend to increase the overall surface

432    area, thereby are more favourable for cell colonization if comparing to the nano-folds (Figure

433    6). However, unlike biofilms spreading on the flat or unitary nano-pillar surfaces, we found

434    that either *S. epidermidis* or *P. aeruginosa* biofilms on rose-petal surfaces were isolated and

435    overall biofilm growth was impaired (Figure 4). Notably, we found that the bacterial growth

436	was lower on unitary nano-pillars after 2 hours, whilst biofilm formation was increased after

437	24 hours if comparing with the rose-petal surfaces. On unitary nano-pillars, the fibres produced

438	by bacteria established connections between isolated cells, and thus may mediate cell-cell

439	communication (Figure S7). However, no large bacterial clusters or dense filamentous

440	structures were found within micro-papillae on rose-petal surfaces (Figure 4). The papillae

441	depth may play an important role as a physical barrier to hinder the development of fibrous

442	network. Therefore, the communication between the neighbouring cell aggregates/clusters that

443	self-developed in each papillae valley may get blocked, and consequently retard biofilm

444	development (Figure 6). Such a hindrance of biofilm development by specific topographically

445	engineered surfaces has been observed previously[7, 60-61]. For example, colloidal crystals of a

446	larger diameter (~1500 nm) can more effectively separate cell bodies than the ones in a

447	diameter of 450 nm, thereby delaying biofilm growth[60]. Other studies have tested biofilm

448	growth on micro-posts (~20×20 μm, pitch~10 μm), similar to the dimension of micro-papillae

449	on the rose-petals[61]. Decreased biofilm growth was observed within the valleys between the

450	unitary micro-posts, while more biofilm was formed on the top of posts (i.e. protruding

451	plateaus)[61]. This indicated that a larger scaled topography size helps to isolate cells while its

452	larger contact area on the top may facilitate more bacterial growth.

453	However, no significant clusters within nano-folds were found, indicating that creating a

454	secondary topography on the microstructure is more effective to delay bacterial growth

455	compared with the bare microstructures. When submerged in water, the trapped air in nano-

456	folds would vanish over time, similar to the lotus-leaf structures, resulting in the transition of

457	Cassie to Wenzel state. Bacterial cells can eventually make contacts with the nano-folds after

458	this region is completely wetted (Figure 6). The dimensions of nano-folds (width ~700 ±100

459	nm, gap ~500 ±150 nm) are similar to the bacterial size. Therefore, either *S. epidermidis* or *P.*

460	*aeruginosa* cells can deposit into the folds and align with the fold structure, especially for *P.*

461	*aeruginosa* (Figure 4& 6). *P. aeruginosa* cells also align within unitary nano-pillars (Figure 5),

462	which maximizes the contact area with the material surfaces. Similar observations have been

463	reported by other researchers, although the underpinning mechanism is not yet clear[10, 62-64].

464	Specific bacterial mutants could be a useful tool to investigate cell alignment and surface

465	structure mediated cell-cell communication, and this will be a target for future work. However,

466	the long and irregular fold ridges can isolate cells via the alignment on rose-petal (Figure

467	S5c&6), and such isolation behaviour is also identical on our nano-pillars with showing the

468	lower biofilm biomass comparing to the flat surfaces. This delayed the formation of cell-cell

469  connections, thereby hindering their communication and constraining bacterial cluster
470  development.
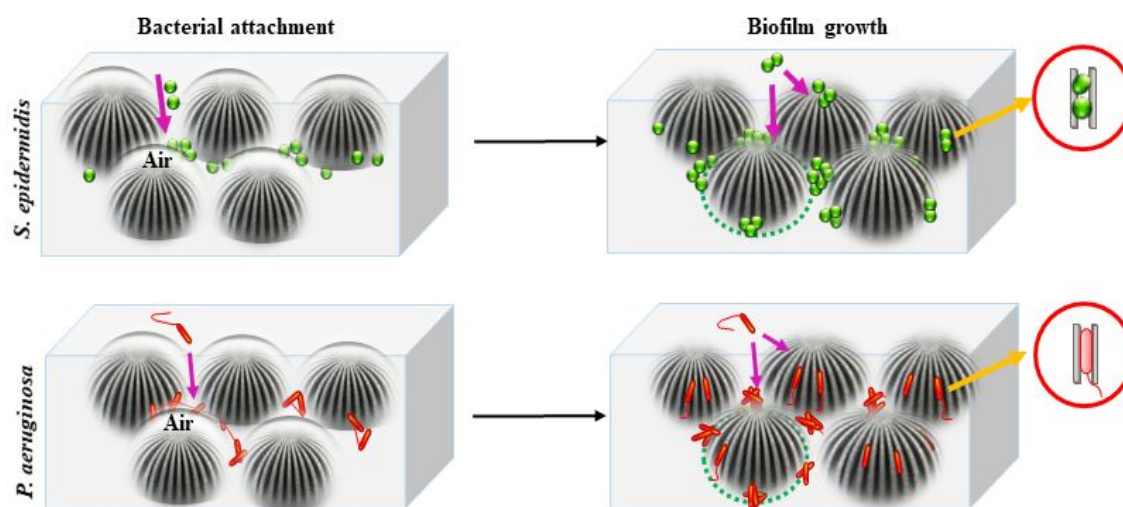


472  **Figure 6.** Hypothesized anti-biofilm mechanisms for the transition from bacterial attachment
473  to biofilm growth on rose petal structured surfaces.

474

475  **CONCLUSIONS**

476  In summary, our study has revealed that rose-petal structured surfaces can delay bacterial
477  attachment and biofilm formation with clinically relevant strains of bacteria. We successfully
478  demonstrated the fabrication of a hierarchical rose-petal structure via a simple UV-curable
479  nanocasting technique, which is cost-effective when compared with fabrication methods like
480  e-beam lithography and nanoimprinting lithography. The rose-petal replicas exhibit a high CA
481  and CAH as a Cassie impregnating wetting state. Similar to superhydrophobic lotus-leaf, the
482  trapped air within nano-folds may hinder the bacterial attachment. While bacteria preferentially
483  form clusters within the valleys of micro-papillae, as they are preferentially wetted and offer
484  more favourable colonization sites when comparing to the nano-folds. We specifically
485  discussed the anti-biofilm mechanism of hierarchical structures under submerged conditions,
486  and the different topography size influence biofilm formation via different mechanisms: micro-
487  papillae blocked the bacterial clusters in between the valleys, limiting the potential for cell-cell
488  communication via fibrous networks, thereby resulting in impaired biofilm growth. At the same
489  time, having a secondary nanostructure (nano-folds) on microstructures can align bacterial cells
490  within the constrained gaps, thereby delaying in developing cell clusters during short term
491  growth of biofilm.

19

492 Rose-petal surfaces have shown potential in parallel and multistep droplet manipulation owing
493 to their high CAH. The hierarchical structures characterized here may be useful for the
494 development of microfluidics and portable/wearable biosensors[65]. In addition, such
495 hierarchical structures can capture and release circulating tumor cells (CTCs) for subsequent
496 analysis[66], exhibiting great potential in biomedical devices. Therefore, this study is a significant
497 step toward the application of rose-petal surfaces where biofilm control is also important.
498 Furthermore, hierarchical structures may be useful to study the roles of microbial cell-cell
499 interactions in biofilm formation. Determining the most effective topography size for
500 controlling biofilm development is an important next step for the development of antifouling
501 surfaces. Future studies will also aim to investigate the anti-biofilm mechanisms in more detail,
502 for example by comparing the anti-biofilm efficacy of rose-petal hierarchical structures with
503 other artificial unitary or hierarchical structures with different scales, investigating bacterial
504 patterning on rose-petal nano-folds and their effects on biofilm formation, and determining
505 whether rose petal replica surfaces are capable of inhibiting growth of biofilms by different
506 species of bacteria.

507

## AUTHOR INFORMATION

509 Corresponding Author

510 * *Jinju Chen: Email: jinju.chen@ncl.ac.uk*

511 Author Contributions

512 All authors contributed to this work. Y.C., S.J., N.R., J.B., H.L., N.J. and J.C. designed the
513 research. Y.C., S.J., performed experiments and acquired the data, and performed the data
514 analysis. L.B. and X.T. conducted the SEM experiments. Y.C., N.J. and J.C. prepared the
515 original draft. All authors reviewed and edited the manuscript. All authors have given approval
516 to the final version of the manuscript.

517

526

## REFERENCES

528  1.      Berne, C.; Ellison, C. K.; Ducret, A.; Brun, Y. V., Bacterial adhesion at the

529  single-cell level. *Nature Reviews Microbiology* **2018,** *16*, 616-27.

530  2.      Mon, H.; Chang, Y.-R.; Ritter, A. L.; Falkinham Iii, J. O.; Ducker, W. A.,

531  Effects of Colloidal Crystals, Antibiotics, and Surface-bound antimicrobials on

532  Pseudomonas aeruginosa Surface Density. *ACS Biomaterials Science &*

533  *Engineering* **2017,** *4* (1), 257-265.

534  3.      Joo, H.-S.; Otto, M., Molecular basis of in vivo biofilm formation by

535  bacterial pathogens. *Chemistry & biology* **2012,** *19* (12), 1503-1513.

536  4.      Bryers, J. D., Medical biofilms. *Biotechnology and bioengineering* **2008,**

537  *100* (1), 1-18.

538  5.      Cao, Y.; Su, B.; Chinnaraj, S.; Jana, S.; Bowen, L.; Charlton, S.; Duan, P.;

539  Jakubovics, N. S.; Chen, J., Nanostructured titanium surfaces exhibit

540  recalcitrance towards Staphylococcus epidermidis biofilm formation. *Scientific*

541  *reports* **2018,** *8* (1), 1071.

542  6.      Mantle, S.; England, N. H. S., Reducing HCAI-What the Commissioner

543  needs to know. *NHS England* **2015,** *8*.

544  7.      Chang, Y.-R.; Weeks, E. R.; Ducker, W. A., Surface Topography Hinders

545  Bacterial Surface Motility. *ACS applied materials & interfaces* **2018,** *10* (11),

546  9225-9234.

547  8.      Mah, T.-F.; Pitts, B.; Pellock, B.; Walker, G. C.; Stewart, P. S.; O'Toole,

548  G. A., A genetic basis for Pseudomonas aeruginosa biofilm antibiotic resistance.

549  *Nature* **2003,** *426* (6964), 306.

550  9.      Li, X.; Cheung, G. S.; Watson, G. S.; Watson, J. A.; Lin, S.; Schwarzkopf,

551  L.; Green, D. W., The nanotipped hairs of gecko skin and biotemplated replicas

552  impair and/or kill pathogenic bacteria with high efficiency. *Nanoscale* **2016**.

553  10.     Friedlander, R. S.; Vlamakis, H.; Kim, P.; Khan, M.; Kolter, R.; Aizenberg,

554  J., Bacterial flagella explore microscale hummocks and hollows to increase

555  adhesion. *Proceedings of the National Academy of Sciences* **2013,** *110* (14),

556  5624-5629.

557  11.     Saison, T.; Peroz, C.; Chauveau, V.; Berthier, S.; Sondergard, E.; Arribart,

558  H., Replication of butterfly wing and natural lotus leaf structures by nanoimprint

559  on silica sol–gel films. *Bioinspiration & biomimetics* **2008,** *3* (4), 046004.

560  12.     Koch, K.; Bhushan, B.; Jung, Y. C.; Barthlott, W., Fabrication of artificial

561  Lotus leaves and significance of hierarchical structure for superhydrophobicity

562  and low adhesion. *Soft Matter* **2009,** *5* (7), 1386-1393.

563    13.    Watson, G. S.; Green, D. W.; Cribb, B. W.; Brown, C. L.; Meritt, C. R.;
564    Tobin, M. J.; Vongsvivut, J.; Sun, M.; Liang, A.-P.; Watson, J. A., Insect
565    analogue to the Lotus leaf: a planthopper wing membrane incorporating a low-
566    adhesion, nonwetting, superhydrophobic, bactericidal, and biocompatible
567    surface. *ACS applied materials & interfaces* **2017,** *9* (28), 24381-24392.
568    14.    Liu, Y.; Choi, C.-H., Condensation-induced wetting state and contact angle
569    hysteresis on superhydrophobic lotus leaves. *Colloid and Polymer Science* **2013,**
570    *291* (2), 437-445.
571    15.    Kumar, C.; Le Houérou, V.; Speck, T.; Bohn, H. F., Straightforward and
572    precise approach to replicate complex hierarchical structures from plant surfaces
573    onto soft matter polymer. *Royal Society open science* **2018,** *5* (4), 172132.
574    16.    Odom, T. W.; Love, J. C.; Wolfe, D. B.; Paul, K. E.; Whitesides, G. M.,
575    Improved pattern transfer in soft lithography using composite stamps. *Langmuir*
576    **2002,** *18* (13), 5314-5320.
577    17.    Wolfe, D. B.; Love, J. C.; Whitesides, G. M., Nanostructures replicated by
578    polymer molding. *Encyclopedia of Nanoscience and Nanotechnology* **2004**.
579    18.    Truong, V. K.; Webb, H. K.; Fadeeva, E.; Chichkov, B. N.; Wu, A. H. F.;
580    Lamb, R.; Wang, J. Y.; Crawford, R. J.; Ivanova, E. P., Air-directed attachment
581    of coccoid bacteria to the surface of superhydrophobic lotus-like titanium.
582    *Biofouling* **2012,** *28* (6), 539-550.
583    19.    Fadeeva, E.; Truong, V. K.; Stiesch, M.; Chichkov, B. N.; Crawford, R. J.;
584    Wang, J.; Ivanova, E. P., Bacterial retention on superhydrophobic titanium
585    surfaces fabricated by femtosecond laser ablation. *Langmuir* **2011,** *27* (6), 3012-
586    3019.
587    20.    Ma, J.; Sun, Y.; Gleichauf, K.; Lou, J.; Li, Q., Nanostructure on taro leaves
588    resists fouling by colloids and bacteria under submerged conditions. *Langmuir*
589    **2011,** *27* (16), 10035-10040.
590    21.    Tang, P.; Zhang, W.; Wang, Y.; Zhang, B.; Wang, H.; Lin, C.; Zhang, L.,
591    Effect of superhydrophobic surface of titanium on staphylococcus aureus
592    adhesion. *Journal of Nanomaterials* **2011,** *2011*, 2.
593    22.    Crick, C. R.; Ismail, S.; Pratten, J.; Parkin, I. P., An investigation into
594    bacterial attachment to an elastomeric superhydrophobic surface prepared via
595    aerosol assisted deposition. *Thin Solid Films* **2011,** *519* (11), 3722-3727.
596    23.    Zhang, X.; Wang, L.; Levänen, E., Superhydrophobic surfaces for the
597    reduction of bacterial adhesion. *Rsc Advances* **2013,** *3* (30), 12003-12020.
598    24.    Lee, C.; Kim, C.-J. C., Maximizing the giant liquid slip on
599    superhydrophobic microstructures by nanostructuring their sidewalls. *Langmuir*
600    **2009,** *25* (21), 12812-12818.
601    25.    Bhushan, B.; Jung, Y. C.; Koch, K., Micro-, nano-and hierarchical
602    structures for superhydrophobicity, self-cleaning and low adhesion.
603    *Philosophical Transactions of the Royal Society A: Mathematical, Physical and*
604    *Engineering Sciences* **2009,** *367* (1894), 1631-1672.

26.    Kim, P.; Kreder, M. J.; Alvarenga, J.; Aizenberg, J., Hierarchical or not? Effect of the length scale and hierarchy of the surface roughness on omniphobicity of lubricant-infused substrates. *Nano letters* **2013,** *13* (4), 1793-1799.

27.    Dai, S.; Zhang, D.; Shi, Q.; Han, X.; Wang, S.; Du, Z., Biomimetic fabrication and tunable wetting properties of three-dimensional hierarchical ZnO structures by combining soft lithography templated with lotus leaf and hydrothermal treatments. *CrystEngComm* **2013,** *15* (27), 5417-5424.

28.    Lorenzetti, M.; Dogša, I.; Stošicki, T. a.; Stopar, D.; Kalin, M.; Kobe, S.; Novak, S. a., The influence of surface modification on bacterial adhesion to titanium-based substrates. *ACS applied materials & interfaces* **2015,** *7* (3), 1644-1651.

29.    Bixler, G. D.; Theiss, A.; Bhushan, B.; Lee, S. C., Anti-fouling properties of microstructured surfaces bio-inspired by rice leaves and butterfly wings. *Journal of colloid and interface science* **2014,** *419*, 114-133.

30.    Dundar Arisoy, F.; Kolewe, K. W.; Homyak, B.; Kurtz, I. S.; Schiffman, J. D.; Watkins, J. J., Bioinspired Photocatalytic Shark Skin Surfaces with Antibacterial and Antifouling Activity via Nanoimprint Lithography. *ACS applied materials & interfaces* **2018**.

31.    Reddy, S. T.; Chung, K. K.; McDaniel, C. J.; Darouiche, R. O.; Landman, J.; Brennan, A. B., Micropatterned surfaces for reducing the risk of catheter-associated urinary tract infection: an in vitro study on the effect of sharklet micropatterned surfaces to inhibit bacterial colonization and migration of uropathogenic Escherichia coli. *Journal of endourology* **2011,** *25* (9), 1547-1552.

32.    Chung, K. K.; Schumacher, J. F.; Sampson, E. M.; Burne, R. A.; Antonelli, P. J.; Brennan, A. B., Impact of engineered surface microtopography on biofilm formation of Staphylococcus aureus. *Biointerphases* **2007,** *2* (2), 89-94.

33.    Green, D. W.; Lee, K. K.-H.; Watson, J. A.; Kim, H.-Y.; Yoon, K.-S.; Kim, E.-J.; Lee, J.-M.; Watson, G. S.; Jung, H.-S., High Quality Bioreplication of Intricate Nanostructures from a Fragile Gecko Skin Surface with Bactericidal Properties. *Scientific Reports* **2017,** *7*.

34.    Watson, G. S.; Green, D. W.; Schwarzkopf, L.; Li, X.; Cribb, B. W.; Myhra, S.; Watson, J. A., A gecko skin micro/nano structure–A low adhesion, superhydrophobic, anti-wetting, self-cleaning, biocompatible, antibacterial surface. *Acta biomaterialia* **2015,** *21*, 109-122.

35.    Diu, T.; Faruqui, N.; Sjostrom, T.; Lamarre, B.; Jenkinson, H. F.; Su, B.; Ryadnov, M. G., Cicada-inspired cell-instructive nanopatterned arrays. *Sci Rep* **2014,** *4*, 7122. DOI: 10.1038/srep07122.

36.    Ivanova, E. P.; Hasan, J.; Webb, H. K.; Truong, V. K.; Watson, G. S.; Watson, J. A.; Baulin, V. A.; Pogodin, S.; Wang, J. Y.; Tobin, M. J.; Lobbe, C.; Crawford, R. J., Natural bactericidal surfaces: mechanical rupture of Pseudomonas aeruginosa cells by cicada wings. *Small* **2012,** *8* (16), 2489-94. DOI: 10.1002/smll.201200528.

23

648  37.    Bhadra, C. M.; Truong, V. K.; Pham, V. T.; Al Kobaisi, M.; Seniutinas,
649  G.; Wang, J. Y.; Juodkazis, S.; Crawford, R. J.; Ivanova, E. P., Antibacterial
650  titanium nano-patterned arrays inspired by dragonfly wings. *Sci Rep* **2015,** *5*,
651  16817. DOI: 10.1038/srep16817.
652  38.    Bandara, C. D.; Singh, S.; Afara, I. O.; Wolff, A.; Tesfamichael, T.;
653  Ostrikov, K.; Oloyede, A., Bactericidal Effects of Natural Nanotopography of
654  Dragonfly Wing on Escherichia coli. *ACS Applied Materials & Interfaces* **2017,**
655  *9* (8), 6746-6760.
656  39.    Hochbaum, A. I.; Aizenberg, J., Bacteria pattern spontaneously on periodic
657  nanostructure arrays. **2010**.
658  40.    Díaz, C.; Schilardi, P.; Salvarezza, R.; de Mele, M. F. L., Have flagella a
659  preferred orientation during early stages of biofilm formation?: AFM study using
660  patterned substrates. *Colloids and Surfaces B: Biointerfaces* **2011,** *82* (2), 536-
661  542.
662  41.    Hsu, L.; Fang, J.; Borca-Tasciuc, D.; Worobo, R.; Moraru, C. I., The effect
663  of micro-and nanoscale topography on the adhesion of bacterial cells to solid
664  surfaces. *Applied and environmental microbiology* **2013**, AEM. 03436-12.
665  42.    Lai, C. Q., Bacterial Attachment, Aggregation, and Alignment on
666  Subcellular Nanogratings. *Langmuir* **2018,** *34* (13), 4059-4070.
667  43.    Feng, L.; Zhang, Y.; Xi, J.; Zhu, Y.; Wang, N.; Xia, F.; Jiang, L., Petal
668  effect: a superhydrophobic state with high adhesive force. *Langmuir* **2008,** *24* (8),
669  4114-4119.
670  44.    Dou, X.-Q.; Zhang, D.; Feng, C.; Jiang, L., Bioinspired hierarchical surface
671  structures with tunable wettability for regulating bacteria adhesion. *ACS nano*
672  **2015,** *9* (11), 10664-10672.
673  45.    Gart, S.; Mates, J. E.; Megaridis, C. M.; Jung, S., Droplet impacting a
674  cantilever: A leaf-raindrop system. *Physical Review Applied* **2015,** *3* (4), 044019.
675  46.    Huhtamäki, T.; Tian, X.; Korhonen, J. T.; Ras, R. H., Surface-wetting
676  characterization using contact-angle measurements. *Nature protocols* **2018,** *13*
677  (7), 1521.
678  47.    McFarland, K. A.; Dolben, E. L.; LeRoux, M.; Kambara, T. K.; Ramsey,
679  K. M.; Kirkpatrick, R. L.; Mougous, J. D.; Hogan, D. A.; Dove, S. L., A self-lysis
680  pathway that enhances the virulence of a pathogenic bacterium. *Proceedings of*
681  *the National Academy of Sciences* **2015,** *112* (27), 8433-8438.
682  48.    Weigert, M.; Ross-Gillespie, A.; Leinweber, A.; Pessi, G.; Brown, S. P.;
683  Kümmerli, R., Manipulating virulence factor availability can have complex
684  consequences for infections. *Evolutionary applications* **2017,** *10* (1), 91-101.
685  49.    Shields, R. C.; Mokhtar, N.; Ford, M.; Hall, M. J.; Burgess, J. G.;
686  ElBadawey, M. R.; Jakubovics, N. S., Efficacy of a marine bacterial nuclease
687  against biofilm forming microorganisms isolated from chronic rhinosinusitis.
688  *PLoS One* **2013,** *8* (2), e55339.
689  50.    Sidorenko, J.; Jatsenko, T.; Kivisaar, M., Ongoing evolution of
690  Pseudomonas aeruginosa PAO1 sublines complicates studies of DNA damage

691 repair and tolerance. *Mutation Research/Fundamental and Molecular*
692 *Mechanisms of Mutagenesis* **2017,** *797*, 26-37.

693 51. MacCallum, N.; Howell, C.; Kim, P.; Sun, D.; Friedlander, R.; Ranisau, J.;
694 Ahanotu, O.; Lin, J. J.; Vena, A.; Hatton, B., Liquid-infused silicone as a
695 biofouling-free medical material. *ACS Biomaterials Science & Engineering* **2014,**
696 *1* (1), 43-51.

697 52. Chuang, Y.-C.; Chu, C.-K.; Lin, S.-Y.; Chen, L.-J., Evaporation of water
698 droplets on soft patterned surfaces. *Soft matter* **2014,** *10* (19), 3394-3403.

699 53. Khedir, K. R.; Kannarpady, G. K.; Ishihara, H.; Woo, J.; Trigwell, S.;
700 Ryerson, C.; Biris, A. S., Advanced studies of water evaporation kinetics over
701 teflon-coated tungsten nanorod surfaces with variable hydrobicity and
702 morphology. *The Journal of Physical Chemistry C* **2011,** *115* (28), 13804-13812.

703 54. Kulinich, S.; Farzaneh, M., Effect of contact angle hysteresis on water
704 droplet evaporation from super-hydrophobic surfaces. *Applied Surface Science*
705 **2009,** *255* (7), 4056-4060.

706 55. Shin, S.; Seo, J.; Han, H.; Kang, S.; Kim, H.; Lee, T., Bio-inspired extreme
707 wetting surfaces for biomedical applications. *Materials* **2016,** *9* (2), 116.

708 56. Azeredo, J.; Azevedo, N. F.; Briandet, R.; Cerca, N.; Coenye, T.; Costa, A.
709 R.; Desvaux, M.; Di Bonaventura, G.; Hébraud, M.; Jaglic, Z., Critical review on
710 biofilm methods. *Critical reviews in microbiology* **2017,** *43* (3), 313-351.

711 57. Busscher, H. J.; van der Mei, H. C., Microbial adhesion in flow
712 displacement systems. *Clinical microbiology reviews* **2006,** *19* (1), 127-141.

713 58. Takahashi, C.; Kalita, G.; Ogawa, N.; Moriguchi, K.; Tanemura, M.;
714 Kawashima, Y.; Yamamoto, H., Electron microscopy of Staphylococcus
715 epidermidis fibril and biofilm formation using image-enhancing ionic liquid.
716 *Analytical and bioanalytical chemistry* **2015,** *407* (6), 1607-1613.

717 59. Rykaczewski, K.; Landin, T.; Walker, M. L.; Scott, J. H. J.; Varanasi, K.
718 K., Direct imaging of complex nano-to microscale interfaces involving solid,
719 liquid, and gas phases. *ACS nano* **2012,** *6* (10), 9326-9334.

720 60. Kargar, M.; Chang, Y.-R.; Khalili Hosseinabad, H.; Pruden, A.; Ducker,
721 W. A., Colloidal Crystals Delay Formation of Early Stage Bacterial Biofilms.
722 *ACS Biomaterials Science & Engineering* **2016**.

723 61. Hou, S.; Gu, H.; Smith, C.; Ren, D., Microtopographic patterns affect
724 Escherichia coli biofilm formation on poly (dimethylsiloxane) surfaces.
725 *Langmuir* **2011,** *27* (6), 2686-2691.

726 62. Dubey, G. P.; Mohan, G. B. M.; Dubrovsky, A.; Amen, T.; Tsipshtein, S.;
727 Rouvinski, A.; Rosenberg, A.; Kaganovich, D.; Sherman, E.; Medalia, O.,
728 Architecture and characteristics of bacterial nanotubes. *Developmental cell* **2016,**
729 *36* (4), 453-461.

730 63. Baidya, A. K.; Bhattacharya, S.; Dubey, G. P.; Mamou, G.; Ben-Yehuda,
731 S., Bacterial nanotubes: a conduit for intercellular molecular trade. *Current*
732 *opinion in microbiology* **2018,** *42*, 1-6.

25

733    64.    Dubey, G. P.; Ben-Yehuda, S., Intercellular nanotubes mediate bacterial
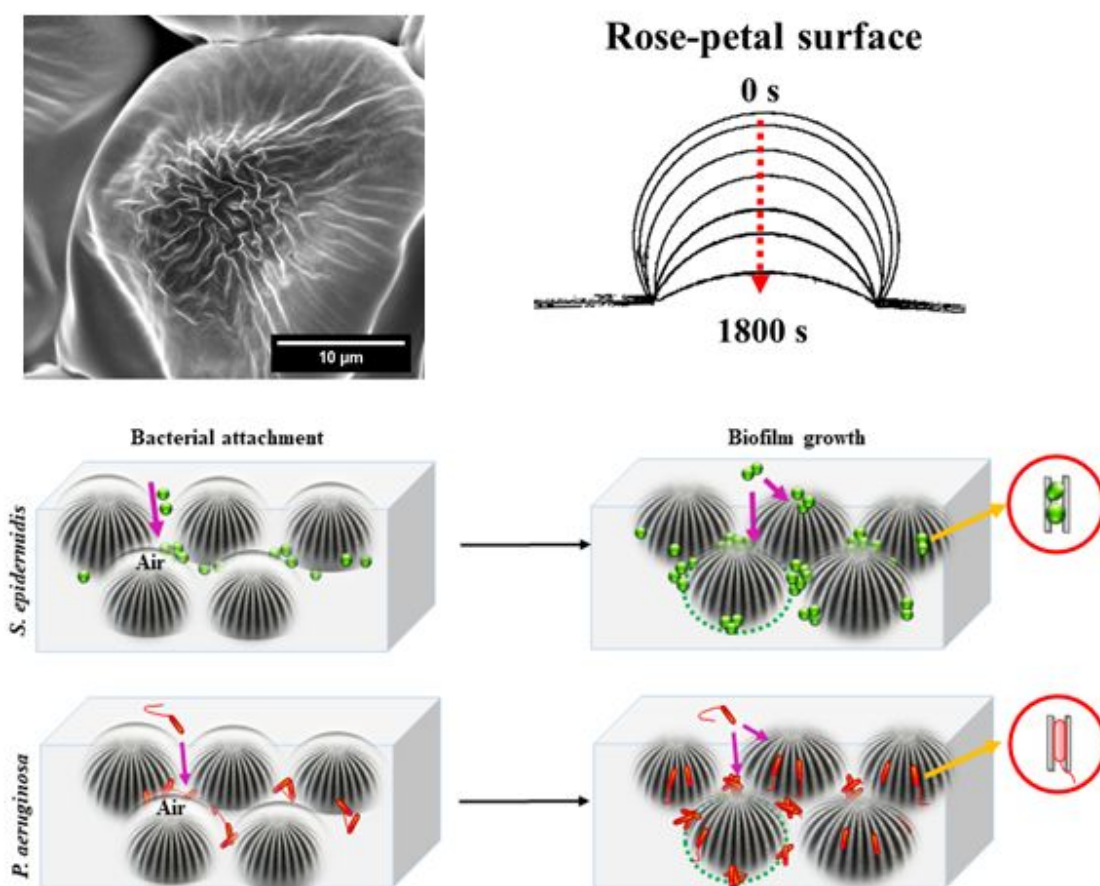734    communication. *Cell* **2011,** *144* (4), 590-600.
735    65.    Wong, W. S.; Nasiri, N.; Liu, G.; Rumsey-Hill, N.; Craig, V. S.; Nisbet, D.
736    R.; Tricoli, A., Flexible transparent hierarchical nanomesh for rose petal - like
737    droplet manipulation and lossless transfer. *Advanced Materials Interfaces* **2015,**
738    *2* (9), 1500071.
739    66.    Dou, X.; Li, P.; Jiang, S.; Bayat, H.; Schönherr, H., Bioinspired
740    hierarchically structured surfaces for efficient capture and release of circulating
741    tumor cells. *ACS applied materials & interfaces* **2017,** *9* (10), 8508-8518.

742

743

744    **Table of Contents Graphic**



745